SNOW DEPTH RETRIEVAL USING KU-BAND INTERFEROMETRIC SYNTHETIC APERTURE RADAR (INSAR)

J.R. Evans [a] and F. A. Kruse [b, c, *]
[a] Department of Meteorology, [b] Physics Department, [c] Remote Sensing Center,
Naval Postgraduate School, Monterey, CA USA 93943

Abstract

Snow accumulation is a significant factor for hydrological planning, flood prediction, trafficability, avalanche control, and numerical weather/climatological modeling. Current snow depth measurement methods fall short of requirements. This research explored a new approach for determining snow depth using airborne interferometric synthetic aperture radar (InSAR). Digital elevation models (DEM) were produced using Multi-pass (monostatic) Single Look Complex (SLC) airborne Ku-band SAR for Snow-Off and Snow-On cases and differenced to determine elevation change from accumulated snow. A perturbation method that isolated and compared high frequency terrain phase to elevation was used to generate DEMs from the InSAR data. Manual snow depth measurements taken to validate the results indicated average InSAR snow depth errors of -8cm, 95cm, -49cm, 176cm, 87cm, and 42cm for six SAR pairs with respect to the measured ground truth. The source of these errors is not fully resolved, but appears to be mostly related to uncorrected slope and tilt in fitted low frequency planes. Results show that this technique has promise but accuracy could be substantially improved by the use of bistatic SAR systems, which would allow for more stable and measurable interferometric baselines.

1. INTRODUCTION

Monitoring seasonal snow accumulation is important as a factor required for evaluation of snow models, short- and long-term snow cover monitoring, and for both military and civilian operations. Improved spatial analysis of snow depth and volume can help decision makers plan for future events and mitigate risk. The use of remote sensing tools provides a way of covering large areas that are difficult to measure directly using other methods. The Naval Postgraduate School (NPS) is using Interferometric Synthetic Aperture Radar (InSAR) to explore snow depth estimation approaches. The Snow Depth Airborne Radar (SNODAR) project uses digital elevation models (DEMs) produced during “Snow-Off” and "Snow-On" conditions utilizing interferometric methods applied to airborne Ku-band Lynx SAR data acquired on a General Atomics Aeronautical (GAA) King Air aircraft. Multi-pass (monotstatic) Single Look Complex (SLC) SAR data are spatially coregistered, SAR interferograms are produced to determine total wrapped phase, the wrapped interferograms are unwrapped, a flat earth correction is applied using a best-fit-plane perturbation model and a low-resolution DEM, and phase is converted to absolute height using linear regression to known elevations. Determination of the Snow-Off and Snow-On DEMs and subsequent subtraction provides an estimate of elevation change caused by snow accumulation for specific locations and an integrated snow volume over a specified area. Manual snow depth measurements and snow analysis were utilized to validate the SAR results in terms of snow depth, water content, and potential snow penetration. Participants in this research included the Naval Postgraduate School, Sandia National Laboratory, General Atomics Aeronautical, The Cold Regions Research and Engineering Laboratory US Army Research and Development Center (CRREL), and Mammoth Mountain California Ski Patrol. Cooperative research is also underway with the German Aerospace Center (DLR) utilizing their X-band SAR satellites (TerraSAR-X/Tandem-X). NPS is exploring future efforts utilizing a single-pass (bistatic) Ka-Band pass airborne system. The ultimate goal is to design operational approaches for regional snow depth determination using airborne and satellite SAR systems.

* *Corresponding author address:* Fred A. Kruse, Physics Department, Naval Postgraduate School, 833 Dyer Rd, Monterey, CA 93943 USA; email: fakruse@nps.edu

2. BACKGROUND

The requirement to measure snow depth over large areas is difficult to satisfy. The primary methods that have been used to-date for snow depth estimation include the Air Force Weather Agency’s Snow Depth and Sea Ice Analysis (SNODEP) model, the use of NASA’s SIR-C/X-SAR missions, the use of ground penetrating radar, and the use of LiDAR.

2.1 SNODEP

The Air Force Weather Agency’s Snow Depth and Sea Ice Analysis (SNODEP) model is the primary tool used today to provide military

operational users with snow depth information. Snow depth estimates are modeled using a combination of passive microwave imagery from the Special Sensor Microwave/Imager Sounder (SSM/IS) and surface observations to include synoptic, meteorological reporting observations (METAR) and Airways and snow depth climatology (AFWA, 2012a, 2012b).

SNODEP makes an initial snow depth estimate based on the previous model run, similar to the approach used in many numerical weather prediction models to establish an initial background field. Once the background field is established, the model incorporates any available surface snow depth observations. It uses an inverse linear weighting scheme to interpolate the data to the closest grid point. Then, in regions without surface reports, SSM/IS algorithms are used to detect snow. If no snow was previously detected, a value of 0.1m of snow depth is automatically assigned. If snow is detected where snow was previously detected, the snow depth estimate is trended toward climatology. If no snow is detected, the estimate for the area remains snow free.

The main strength of SNODEP is its ability to provide a global view of snow coverage. It does, however, have several weaknesses. Due to the inherent resolution of the SSM/IS satellite; SNODEP's best resolution is 25km (Foster 2011). This spatial resolution typically is not adequate to provide the detail that operational users require. Its grid can also be too large to adequately estimate the snow depth in smaller watersheds, especially in complex terrain such as mountainous regions. In addition, the in-situ observations are extremely limited and the observations tend to be concentrated in more developed countries like the U.S. Many stations record snowfall, which should not be confused with snow depth on the ground. Mechanisms such as settling, melting, sublimation, and movement of snow by wind make the snowfall measurements a poor estimate of snow depth. Thus, inadequate characterization of spatial variability is a big concern. To make up for this poor coverage of in-situ observations the SSM/IS passive microwave satellite is used to determine the snow depth everywhere else. SSM/IS does this by using a correlation coefficient between the microwave brightness temperature and snow depth. This coefficient assumes snow crystal grain size, and that the snow is dry or refrozen. Failure of either of these assumptions can negatively affect the accuracy of the model. Furthermore, snow depth estimates from the SSM/IS are limited to depths of 40cm or less. The snow depth algorithm becomes unreliable when the snow depth exceeds 40cm (Northrop Grumman 2010).

2.2 SIR-C/X-SAR

The Spaceborne Imaging Radar-C/X-band Synthetic Aperture Radar (SIR-C/X-SAR) flew two missions on NASA's space shuttle in 1994, imaging 57.6 million square miles, or approximately 14 percent of the Earth's surface (Stofan et al. 1995; JPL, 2012a, 2012b). The space shuttle launched with three different synthetic aperture radar (SAR) antennas. These included L-band (23.5cm wavelength), C-band (5.8cm wavelength), and X-band (3cm wavelength) antennas. The L and C bands were also capable of polarimetric measurements. The use of the three different bands allowed collection of information about the Earth's surface at multiple scales, which had never been possible before with only single band SAR systems.

Snow characteristics have a large effect on the backscattering of radar emissions, thus a multifrequency, polarimetric SAR system has several advantages over other sensors for snow depth estimation. Parameters affecting what can be measured include (Shi and Dozier, 1996):

1. Sensor characteristics, to include frequency/wavelength, polarization, and viewing angle
2. Snow pack parameters to include snow density, depth, particle size, size variation, liquid water content (stickiness), and stratification
3. Ground parameters to include dielectric and roughness parameters

Differences in backscattering properties by different radar wavelengths on the snow pack can be leveraged to determine the physical characteristics of the snow pack and the underlying ground. All three of the SIR-C/X-SAR wavelengths are assumed to penetrate into the snowpack. Based on electro-magnetic scattering theory, for a given material, there is a direct relationship between the wavelength and the depth of penetration (Richards, 2009). With that in mind, there should be an increase in backscattering moving from the L-band radar down to the X-band radar. This fact was used by Shi and Dozier (2000a, 2000b), to retrieve snowpack properties. They first used polarized data from the L-band radar to determine snowpack density. L-band proved to be a long enough wavelength that the backscatter from the

snowpack was negligible. The entire radar return therefore came from the ground below the snow pack. Despite the lack of backscatter from the snow, they were able to capitalize on the fact that the snow pack caused a shift in refraction in the incidence angle of the radar pulse. The extent of the refraction was dependent on the density of the snow pack. Furthermore, there was a difference in both the magnitude and relation between the VV and HH polarizations. By modeling this interaction, they were able to derive the snowpack's density.

Due to the large variability in density in snowpacks, however, the density alone is not enough to estimate other characteristics of the snow pack such as snow depth or snow water equivalent (SWE). To do this Shi and Dozer (2000a, 2000b) used data from both the C-band and X-band radars. Both C-band and X-band radar pulses have different volume scattering properties. This fact was used to model the particle size and expected magnitude of the scattering. Both bands were assumed to penetrate to the ground in addition to the volume scattering, which added an additional component to the overall return. This was accounted for, however, by using the ground roughness and dielectric properties determined from the L-band radar.

This approach of using a combination of all three SAR bands showed very positive results and has stood up well to ground validation. While this technique has shown great potential, there are not, however currently any spaceborne or airborne sensors with the appropriate configuration to take advantage of this technique.

2.3 Ground Penetrating Radar

There have also been attempts to use ground penetrating radar (GPR) to address the issue of determining snow depth and other snowpack characteristics (Marshall et al., 2005). Frequency modulated continuous wave (FMCW) radar has proven to be the most successful of the GPRs for snow study. The FMCW radar works similarly to a standard radar system in that it times the pulse to determine range. It however uses a broad band width that results in a greater theoretical vertical resolution as compared to a standard GPR (Yankielun et al. 2004). This greater vertical resolution is quite important if you want to determine snow pack stratigraphy, which can be particularly important for avalanche prediction. Ground penetrating radars are typically deployed for snow pack analysis either by hand or by towing them behind a snowmobile. Recently they have been deployed using low flying helicopters with some success (Marshal et al. 2008).

Overall, the use of these FMCW radars has been quite successful at determining snowpack characteristics; in particular those characteristics that concern avalanche experts in focused areas. They are not, however, suited for covering larger areas. Deploying them on the ground, whether by hand or being towed behind a snowmobile or snowcat, does not provide nearly the spatial coverage provided by airborne systems. Ground deployment is also restricted by complex terrain. The use of the GPR by helicopter also has drawbacks. The systems used to-date have a fairly broad footprint. That means that as the GPR platform altitude increases, the area covered by the footprint also increases dramatically. Everything in the footprint is treated as a single return per pulse. The more the terrain varies within the footprint, the less reliable the measurements. Work done by Marshal et al. (2008) has shown that altitudes greater than 100ft above the ground make the data unreliable. Performance can be worse in areas where there are steep slopes. There are plans to try to use a FMCW GPR with a narrower beam to address this issue. With such restrictions, however, operational airborne collections in complex terrain are not currently possible.

2.4 LiDAR

Light Detection and Ranging (LiDAR) is another method that has been explored to estimate snow depth. LiDAR is based on measuring the time required for a pulse of light to travel to a target and then return to determine range (Hodgson et al. 2005). This can be used to build either 2-dimensional or 3-dimensional scenes. To determine snow depth, the scene is imaged with and without snow and then differenced, resulting in a snow volume and snow depth estimate at each specific point. The use of LiDAR has a lot of advantages. The first is that it can be used to cover large areas in an unobtrusive manner. It is also highly accurate, with accuracies down to the millimeter level in some cases (Osterhuber et al. 2008).

LiDAR has been deployed two different ways to determine snow depth. The most accurate way is to deploy the LiDAR system on the ground. Osterhuber et al. (2008) used a ground based unit that could either be placed on the ground or fixed to a surveyor's tripod. In a snow pack with an average depth of just over two meters the LiDAR averaged a mean difference between manual and LiDAR measurements of 5.7 cm. While the use of

the ground-based system has potential, it also has some drawbacks. Systems currently being used are range-limited to about 1000 meters. Also, to generate a 3-D image, either multiple sensors are required, or the LiDAR has to be moved to different scanning locations. Furthermore, LiDAR becomes ineffective with any obscuring weather phenomena such as clouds, fog, or precipitation. This system may prove to be a great way of measuring snow depth at fixed locations but is not a good option for large regions of land or remote areas where a ground-based unit has not been placed.

The second way to deploy LiDAR is to operate the system from either an airborne or a spaceborne platform. Airborne LiDARs, also known as laser altimetry, are much better suited to cover large regions or remote areas than the fixed based systems (Hodgson et al. 2005). Airborne LiDAR depends on knowing the speed of light, the location of the laser emitter, and being able to time the laser pulse transmission to reception time. These data, like the ground based systems, can be used to generate a 3-D image or terrain model with a resolution at sub-meter level (Hopkinson et al. 2004). This has the same restriction as the ground based system in the fact that the laser path has to be free of visual obscurations. Accuracy also depends on the ability to position the aircraft to a high degree of x, y, z accuracy, which can potentially be problematic. Furthermore, there are a limited number of platforms that are currently equipped to perform this task.

2.5 InSAR DEM Subtraction

The research summarized here is a first step towards developing methods for determining snow depth utilizing InSAR technology. The approach is similar to LiDAR, however, snow depth is estimated by generating DEMs using SAR interferometry followed by subtraction of Snow-On from Snow-Off elevations. SAR has the advantage over LiDAR of being able to pass freely through most atmosphere conditions and through visible obscurations such as clouds and precipitation, allowing measurement of surface characteristics where optical wavelengths would be either absorbed or scattered. These obscurations are common during winter and can be a limiting factor for the use of laser-based systems for snow depth estimation.

From an operational standpoint, InSAR has another advantage. There are both current and planned satellite SAR systems that could be applied to the snow depth measurement problem, and numerous airborne platforms currently carry SAR for other purposes, most notably the MQ-1 Predator and MQ-9 Reaper (General Atomic Aeronautical 2012). Many of these can potentially be adapted for operational InSAR snow depth determination beyond what is currently available using other methods.

Radar uses radiation emitted from an antenna in the microwave region of the electromagnetic (EM) spectrum. This emitted energy travels to a target and is then reflected back to the original, or in some cases an alternate antenna. The time it takes this radiation to travel the distance to and then back from the target is measured. Using the speed of electromagnetic propagation, this allows an estimate of the range to the target (Carrara et al. 1995). The wavelengths most commonly used in radar remote sensing are on the order of 1.5cm to 1m, or approximately 20GHz to 300MHz (Richards 2009). This frequency range is broken down into bands with L- (1–2 GHz), C- (4–8 GHz), and X-bands (8–12 GHz) as the most commonly used for remote sensing. This study used a slightly higher frequency Ku-Band (12–18 Ghz) radar.

InSAR capitalizes on the capability to measure the phase angle of the SAR return. The transmitted phase is known and the return phase can be measured. This allows determination of relative distances from the sensor to the ground. When these distances are measured from two different locations (a change in the radar's position), then topography or topographic displacement can be determined (Richards 2009). This is the basis of InSAR illustrated in Figure 1 and the following equations from Richards (2009) with some modifications.

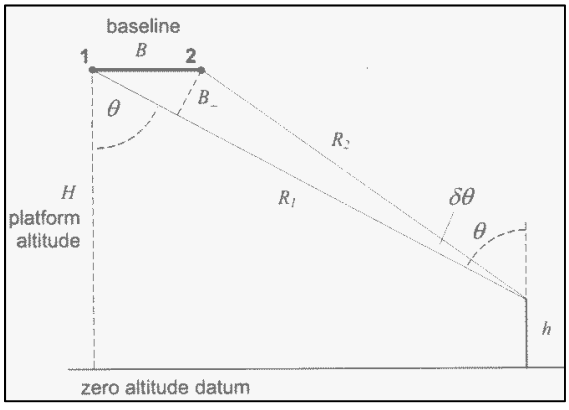

Figure 1: Basic geometry for single baseline SAR interferometry. "R1" and "R2" are the respective ranges from antennas 1 and 2. "B" represents the baseline between the two antenna locations. "B⊥" is the orthogonal baseline between the two radar beam paths. "θ" and "δθ" represent the incidence angle and the change in incidence angle respectively (Richards 2009).

The difference in the path lengths "R_1" and "R_2" in terms of the phase and a given baseline and incidence angle of "B" and "θ" respectively can be derived as:

$$R_1 = R_2 \cos \delta\theta + B \sin \theta \quad (1)$$

δθ is assumed to be approximately 0 using the plane wave approximation. The plane wave approximation considers the change in the incidence angle to approximate 0 when the target is infinitely far away when compared to the length of orthogonal baseline. This results in:

$$R_1 = R_2 + B \sin \theta \quad (2)$$

Therefore

$$\Delta R = R_1 - R_2 = B \sin \theta \quad (3)$$

The difference in phase angle "Δϕ" associated with the change in path length "ΔR" between the two passes can then be given as

$$\Delta\phi = \frac{4\pi B \sin\theta}{\lambda} \quad (4)$$

This difference in phase angle is referred to as *interferometric phase angle* Δϕ. Δϕ can be obtained directly by simply imaging an area twice and taking the difference of the two recorded phases. The next step is to determine the relationship between the topographic height "h" and the incidence angle in order to get the phase to height ratio (Figure 2).

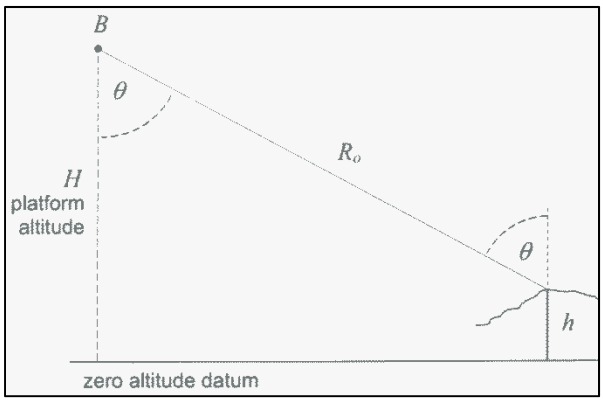

Figure 2: Determining the relationship between topographic height "h" and incidence angle "θ" with a platform altitude of "H" and range to the target of "R_0" (Richards 2009).

From Figure 2, if "H" is the total height above an assumed altitude, and "R_0" is the range to the target, observe that

$$h = H - R_0 \cos\theta \quad (5)$$

Taking the partial derivative of the topographic height with respect to the incidence angle results in

$$\frac{d(h)}{d\theta} = R_0 \sin\theta \quad (6)$$

Then taking the partial derivative of the interferometric phase angle Δϕ with respect to the incidence angle also results in

$$\frac{d(\Delta\phi)}{d\theta} = \frac{4\pi B \cos\theta}{\lambda} \quad (7)$$

Combining equations (12) and (13) results in

$$\frac{d(\Delta\phi)}{dh} = \frac{d(\Delta\phi)}{d\theta}\frac{d\theta}{d(h)} = \frac{4\pi B \cos\theta}{\lambda R_0 \sin\theta} \quad (8)$$

We now have an expression for the change in (10)
interferometric phase with respect to the change in topographic height. Taking it one step further to make it more user friendly results in

$$\frac{d(\Delta\phi)}{dh} = \frac{4\pi B_\perp}{\lambda R_0 \sin\theta} = \frac{4\pi B_\perp \cos\theta}{\lambda (H-h)\sin\theta} \quad (9)$$

So as long as the incidence angle is known, the elevation above some known reference height (H-h) and the orthogonal baseline, the rate of change in elevation across an interferometric phase diagram per change of radian can be predicted. An interferometric phase factor α_{IF} can be defined as

$$\alpha_{IF} = \frac{dh}{d(\Delta\phi)} \quad (10)$$

and the height of a specific pixel will be given by

$$h(x,y) = \alpha_{IF}\Delta\phi(x,y) + CONSTANT \quad (11)$$

Equation (11) enables the generation of a DEM from InSAR image pairs. The ability to use InSAR to generate DEMs is the basis for this research. High resolution InSAR DEMs generated during Snow-On conditions were subtracted from an InSAR Snow-Off DEM to estimate the snow depth utilizing airborne SAR.

APPROACH AND METHODS

This research used airborne SAR data in an approach similar to that taken for airborne LiDAR determination of DEMs. InSAR, was used instead of laser altimetry to map both the bare ground and the snow covered ground. Snow cover effectively acts to change the elevation of the surface. Taking the difference between the two DEMs, Snow-On and Snow-Off, allows determination of snow depth and snow volume over a specified area. This section summarizes the study area, ground validation measurements, and the methods used to extract DEMs from the InSAR data for snow depth determination.

3.1 Site Selection

Selection of the study site included requirements for sufficient snow depth, being relatively obstacle free, a clear view of sky, relatively flat (i.e. no steep slopes relative to the SAR resolution), accessibility, and being within the General Atomics flight radius centered in San Diego, CA. It should be noted that the first criterion of sufficient snow depth played a major role in site selection. There were not many viable options due to the low snow fall in the 2011-2012 winter season when the Snow-On measurements were made. Mammoth Mountain, CA (Figure 3) ultimately met the requirements better than any other location. Eight possible data collection locations were identified. SAR data were ultimately only collected for one site, "Elysian Fields".

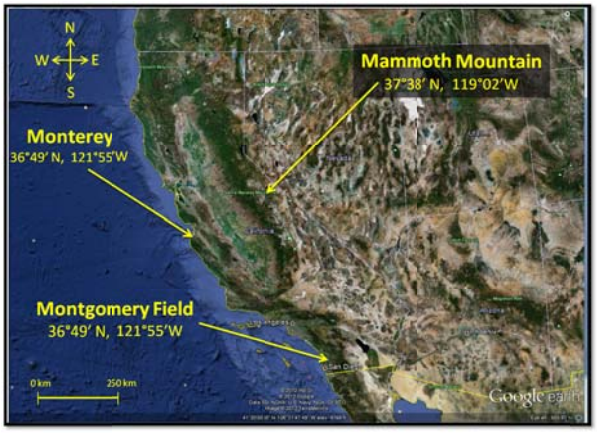

Figure 3: Image-Map showing location of study area (Mammoth Mountain, CA) with respect to the General Atomics Aeronautical (GAA) home airfield near San Diego, CA (Google Earth, 2012).

3.2 On-Site Ground Control and Validation

Custom-designed field-portable 25dBsm trihedral reflectors were deployed at selected ground locations in the collection area during both Snow-On and Snow-Off SAR collections to provide ground control for radiometric calibration and geometric correction of SAR data. Four corner reflectors (CR) were placed on a 100m east-west by 80m north-south grid centered on the Elysian Fields site coordinates.

The first SAR data collect was done during Snow-On conditions, so the snow was excavated to the ground at each corner reflector location to emplace the tripods. The GPS locations were recorded and a stake was placed to mark the location. The stake was critical to allow for return of the reflectors to the same location during the Snow-Off SAR collection. The snow pits dug for the corner reflectors varied between 1.5 to 2.3 meters in snow depth at this collection site. CR were pointed due south or 167° magnetic and with an elevation angle of -13° to correspond with SAR collection parameters and planned flight-lines.

To ensure that the SAR snow depth retrieval techniques' accuracy could be tested, in-situ snow depth was measured concurrently with the Snow-On data collection. These measurements were made using a 1cm graduated avalanche probe immediately after the data acquisition. Due to the disturbed snow directly between the corner reflectors, the measurements were taken approximately every 20 meters within the box outlined by the reflectors. A total of 16 measurements were taken in a roughly 80x80m grid. The in-situ snow depth grid extended outside of the planned analysis area marked by the corner reflectors to the south. In addition to these measurements, random measurements were taken further south of the planned verification area. These measurements extended into the tree-line to help provide insight to the impacts of foliage on this method. All the snow depth measurement locations were recorded using GPS along with calculated GPS error. In addition to these snow depth measurements, a snow pit was dug concurrently with the SAR collection for snow analysis near the northeast CR. It included temperature readings, crystal size and type, and density measurements throughout the column.

3.2 SAR Data Collection

The SAR data collection for this research was done using a Lynx II Ku-band radar (Tsunoda et al. 1999) mounted to a King Air aircraft. General Atomics Aeronautical (GAA), the manufacturer of the Lynx system, agreed to fly collection missions

to generate the raw radar datasets necessary for this research. The radar itself is a Ku-band radar that operates at a 15.2-18.2GHz frequency with a wavelength of 1.8cm. The maximum slant range of this system is 30km. There are multiple ground resolution options, to include 0.1, 0.3, 1.0, and 3.0m. Table 1 indicates the SAR images used in this study.

SAR Image number	Date	Time	Surface Condition
01	3 April 2012	18:47 Z, 10:47 L	snow covered
02	3 April 2012	18:55 Z, 10:55 L	snow covered
03	3 April 2012	19:04 Z, 11:04 L	snow covered
04	3 April 2012	19:00 Z, 11:00 L	snow covered
21	13 July 2012	17:58 Z, 10:58 L	bare
22	13 July 2012	18:05 Z, 11:05 L	bare

Table 1: Four usable Snow-On and two useable Snow-Off SAR images were acquired at 0.1m spatial resolution. These images enabled calculation of six Snow-On and one Snow-Off interferometric pairs.

The radar can be operated in different modes to include spotlight, strip-map, and coherent change detection (Tsunoda et al. 1999). For the purposes of this research, multiple passes were made at both the 0.1 and 0.3m resolutions using the spotlight mode. Both Snow-On and Snow-Off collections were flown on 3 April 2012 and 13 July 2012 respectively. The actual flights were flown at a flight level of 5330m and approximately 10km to the south of the collection area with the radar looking north.

3.3 *DEM Generation and Snow Depth Determination*

The Lynx InSAR data were processed to DEMs using a combination of standard InSAR processing approaches and a new method termed "Best Fit Plane Removal" (BFPR) (Figure 4). Standard InSAR processing steps (Rosen, 2009) including single look complex (SLC) image generation, image registration between a Master and Slave SAR image, interferogram generation using multiplication of the Master by the complex conjugate of the Slave, coherence determination, and phase unwrapping using the branch cut method (Goldstein et al. 1988) were applied to the Lynx SAR image pairs used for this research.

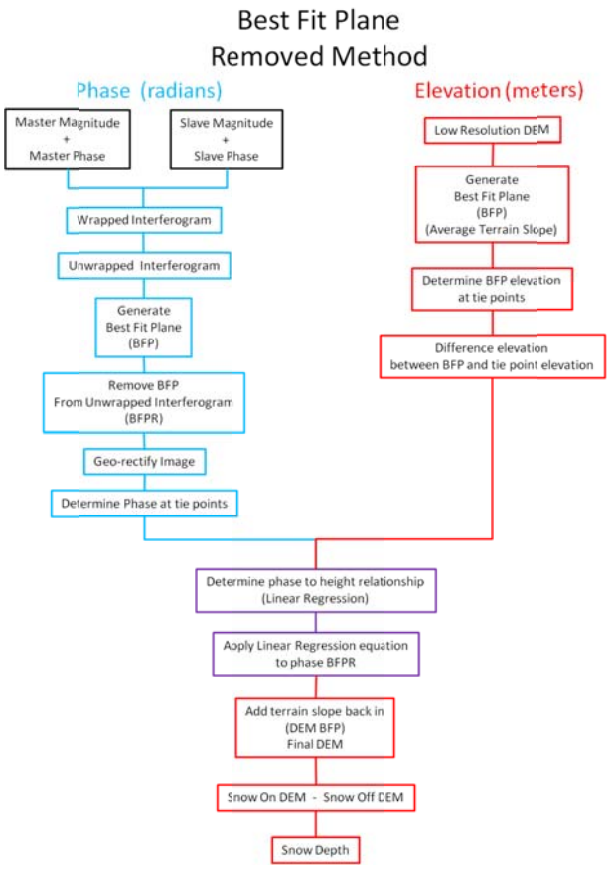

Figure 4: Best Fit Plane Removed method flow chart.

Normally, SAR acquisition baseline information is used to remove Flat Earth phase from the total phase to get at the topography (Richards, 2009; Rosen, 2009), however, in the case of the Lynx airborne data, we determined that uncertainties in 3-dimensional (x, y, z) aircraft positioning and ground targets made accurate calculation of the baselines extremely difficult, therefore, we designed and implemented the innovative BFPR alternate approach (Evans, 2013).

Four usable Snow On and tw

BFPR is best described from a perturbation or decomposition perspective. As used in the following equations, variables with an over-bar represent the mean of that variable while the "prime" symbol or accent mark represents the deviation of the value from a particular mean. In the following equations "$\Delta\phi_{total}$" represents the total phase or the unwrapped interferometric phase, "$\Delta\phi_{flat\_earth}$" represents the flat earth phase.

An unwrapped interferogram is made up of both flat earth and terrain phase as is seen in (12) where "$\Delta\phi z$" represents the phase associated with the terrain (simplified from Richards, 2009).

$$\Delta\phi_{total} = \Delta\phi_{flat\_earth} + \Delta\phi_z \quad (12)$$

From a perturbation perspective, the flat earth phase is

$$\Delta\phi_{flat\_earth} = \Delta\bar{\phi}_{flat\_earth} + \Delta\phi'_{flat\_earth} \quad (13)$$

The flat earth phase, however, is a plane and has no perturbation. Therefore it reduces down to

$$\Delta\phi_{flat\_earth} = \Delta\bar{\phi}_{flat\_earth} \quad (14)$$

The terrain phase from a perturbation perspective is

$$\Delta\phi_z = \Delta\bar{\phi}_z + \Delta\phi'_z \quad (15)$$

Unlike the flat earth phase, there are variations throughout the image. "$\overline{\Delta\phi_z}$" represents the average slope of the terrain and "$\Delta\phi_z$'" is the variation or perturbation from that average slope.

By replacing (14) and (15) into (13), the total phase can now be given as

$$\Delta\phi_{total} = \Delta\bar{\phi}_{flat\_earth} + \Delta\bar{\phi}_z + \Delta\phi'_z$$

or (16)

$$\Delta\phi_{total} = \Delta\phi_{flat\_earth} + \Delta\bar{\phi}_z + \Delta\phi'_z$$

Taking the best fit plane of the total phase is the same as finding the average slope of the phase image and is now given by

$$\Delta\bar{\phi}_{total} = \Delta\bar{\phi}_{flat\_earth} + \Delta\bar{\phi}_z \quad (17)$$

Subtracting the BFP or (17) from the total phase yields

$$\Delta\phi_{total} - \Delta\bar{\phi}_{total} = \Delta\phi_{flat\_earth} + \Delta\bar{\phi}_z + \Delta\phi'_z - \Delta\phi_{flat\_earth} - \Delta\bar{\phi}_z = \Delta\phi'_z \quad (18)$$

Equation (18) represents the BFPR terrain (in phase space) and demonstrates that subtracting the BFP from the total phase results in only the terrain perturbations or terrain that deviates from the mean slope (Figures 5 and 6).

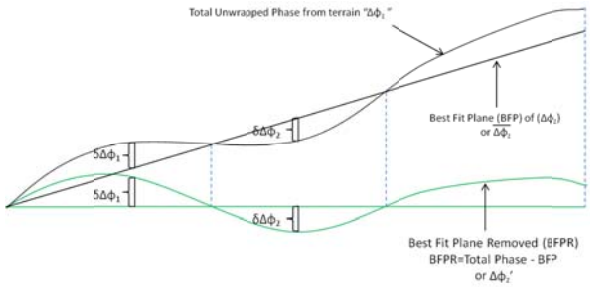

Figure 5: The Best Fit Plane Removed (BFPR) method subtracts the best fit plane (BFP) from the total unwrapped phase. The BFPR isolates the portion of the total unwrapped phase that is due to the deviation of the terrain from the average slope of the terrain and is signified as "$\Delta\phi_z$' " or the equivalent "$\delta\Delta\phi$".

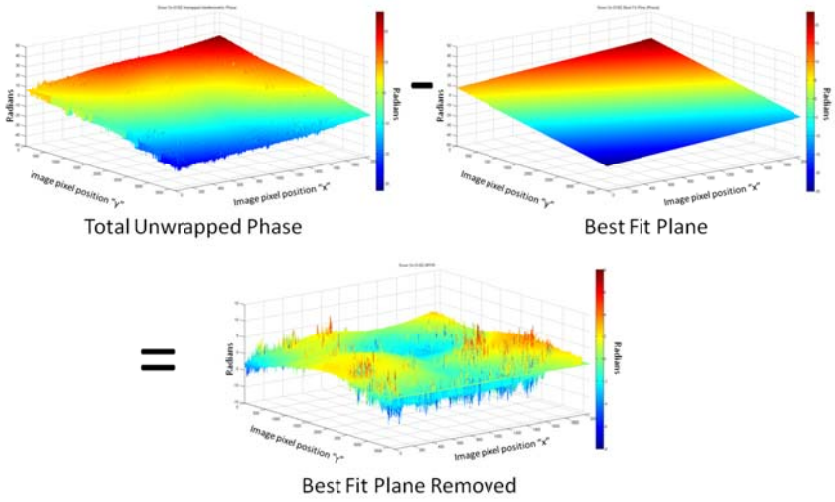

Figure 6: Path to the BFPR. Mammoth Mountain study site, (37°37.7'N, 119°02.7'N), Snow-On pairs 01/02 results. Upper left plane is a 3D perspective view of the Snow-On unwrapped interferogram, the total unwrapped phase. Upper right plane is the best fit plane (BFP) generated from that interferogram, and bottom center plane is the result of subtracting the BFP from the total unwrapped phase. North is to the top-center edge of the perspective views.

Being able to generate a best fit plane from the unwrapped interferogram is important because it facilitates the isolation of the phase produced by high frequency terrain. This approach effectively removes the flat earth phase and the average slope phase as shown in equation (18). Summarizing (Figure 4), the approach requires generation and removal of a BFP from the unwrapped total phase image (Figure 6); determination of a BFP average slope from a low resolution DEM, differencing the elevations of known ground control points and corresponding elevations in the BFP DEM slope image, calculation and application of the phase to elevation relation using a linear regression to convert the BFPR phase image to elevation, and adding back in the low resolution slope (Figure 7); and then subtracting the DEMs determined during Snow-Off and Snow-On conditions to get to estimated snow depths on a per-pixel basis (Figure 8).

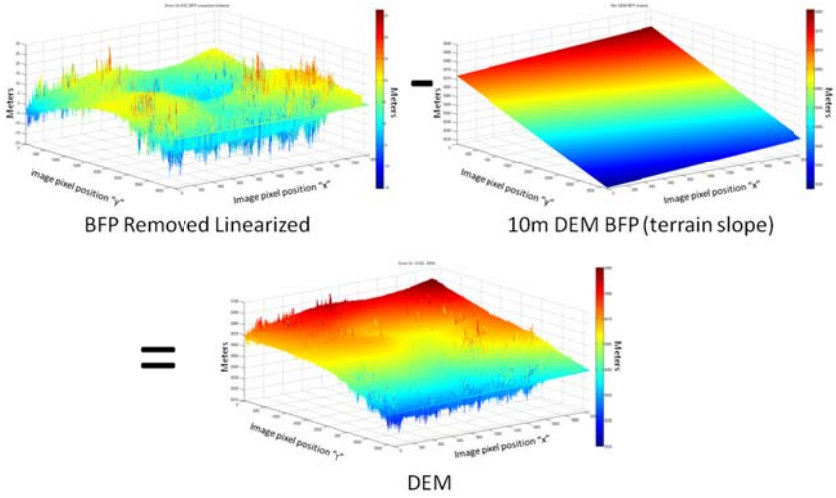

Figure 7: Adding the BFPR after it has had the linear regression equation applied to the low resolution DEM BFP (terrain slope in meters) results in a DEM that is measured in meters. Mammoth Mountain study site, (37°37.7'N, 119°02.7'N), Snow-On pairs 01/02 results. North is to the top-center edge of the perspective views.

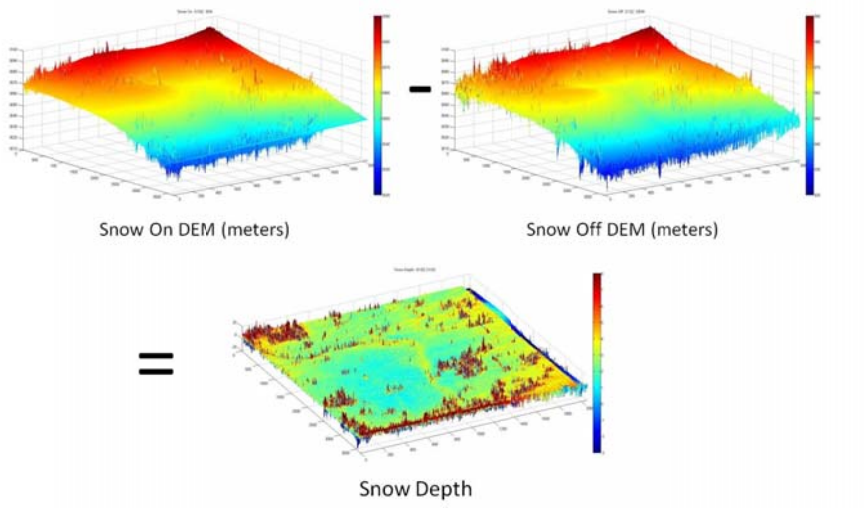

Figure 8: Subtracting the Snow-Off DEM from the Snow-On DEM results in a snow depth image. Mammoth Mountain study site, (37°37.7'N, 119°02.7'N), Snow-On pairs 01/02 results. North is to the top-center edge of the perspective views.

It is important to note that the BFPR is in phase space and must be converted to elevation to be of any use in snow depth estimation. Highly accurate elevations recorded using a survey grade GPS at the corner reflector locations for the Mammoth Mountain site were used to calculate the relation between phase and elevation by comparing the measured elevations to the elevations at those locations relative to the average slope as determined from the low resolution (10m) DEM. Richards (2009) showed that the phase to elevation relationship is linear, therefore, a linear regression between the phase and elevation results in an equation that can now be applied to the entire scene to convert to terrain height. Figure 9 shows the locations of the known elevations (CR) with respect to the 01/02 BFPR image. The linear regression between the phase and elevation for these four points is shown in Figure 10. Application of the regression to the entire BFPR image on a pixel-by-pixel basis results in a DEM based on perturbation of the terrain from the average slope "the "Best Fit Plane Removed and Linearized" (BFPRL) image. Adding the BFPRL image to the previously calculated mean slope from the low resolution DEM results in a new DEM at the same high spatial resolution as the SAR image (Figure 7).

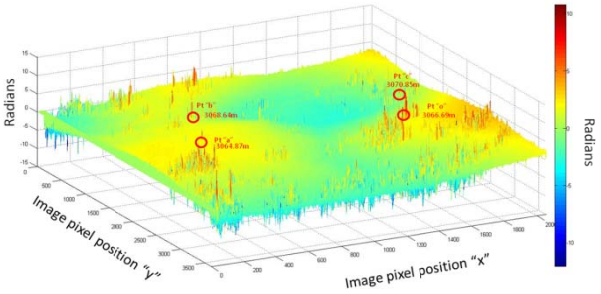

Figure 9: Perspective view of BFPR with CR tie points and accompanying elevations depicted. Mammoth Mountain study site, (37°37.7'N, 119°02.7'W) 01/02 SAR image pair.

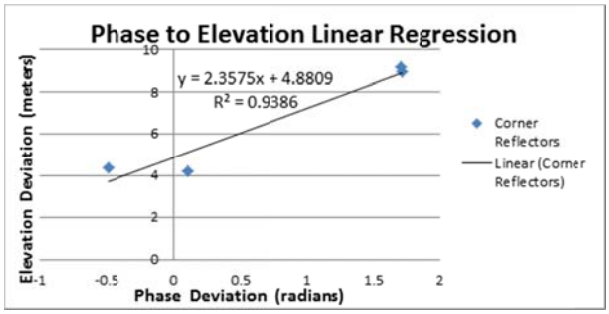

Figure 10: Linear Regression for Snow On 01/02 SAR image pair shows the relationship between the phase and elevation.

3. RESULTS AND ANALYSIS

4.1 Snow Depth Results

Snow depth was calculated utilizing a total of six Snow-On SAR image pairs with varying results. Manual snow depth measurements taken during the field deployment were compared to the SAR-determined snow depths to determine their accuracy. As previously described, the field measurements were measured on a 20m grid bounded by the corner reflector locations. Unfortunately, those measurement locations were recorded with a standard consumer-grade GPS, and this meant that the location accuracy was not the same as that of the corner reflector survey. The estimated accuracy of the snow depth locations was recorded to be on the order of four meters horizontal (x, y). Because of the location accuracy limitations imposed on the field snow measurements, an average snow depth was calculated for a radius of five meters around the recorded locations (Figure 11).

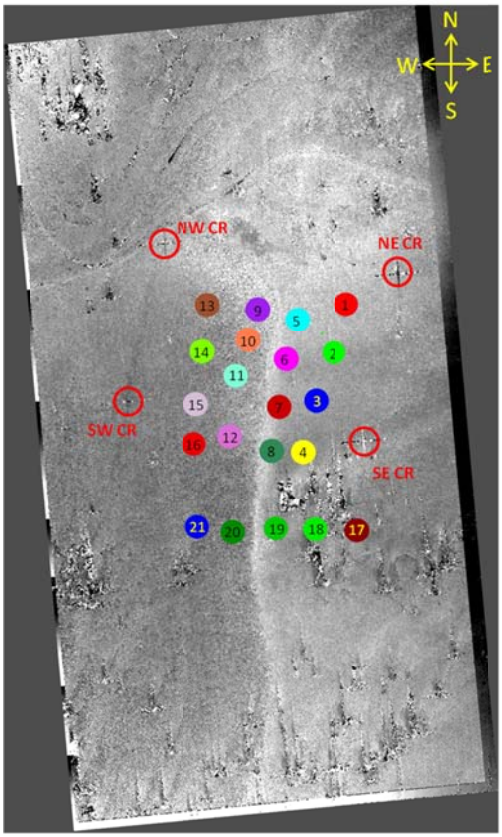

Figure 11: Manual snow depth measurements were taken throughout the scene and are represented by the circles in the above snow depth image. The circle size also demonstrates the 5m radius area that was used to average the snow depth in that location. Corner reflector locations are also shown and labeled (red outlined circles). Mammoth Mountain study site (312 x 176m), (37°37.7'N, 119°02.7'W), SAR pair 01/02.

Figure 12 shows several of the InSAR snow depth images calculated using the BPFR method. Most depths are in the 0 – 2.5m range, with some obvious errors due to the interaction of SAR with trees and other obstacles. Pair 02/03 shows anomalous results (Figure 12C). Examination of the summary results in Table 2 shows widely varying snow depth errors. Table 2 averages all 16 snow depth locations from Figure 11 for each of the six SAR image pairs. It is important to note that in some cases, image pair 01/02 in particular, positive and negative error values average to give a lower average error. Furthermore, high and low coherence locations are mixed in these averages.

The varying snow depth error results seen in Table 2 do not, however tell the whole story. Each of the different SAR image pairs tend to show either a high or low average error rather than all the pairs having a bias in the same direction. While it is not quite clear where these biases are coming from, it is believed that they are either most likely related tilt to and slope differences in the BFP calculations. There are two noted biases. The first is the overall high/low bias. In the pairs that have been computed, two pairs have a high bias for snow depth (01/03, 02/03), and the other four have a low bias (01/02, 01/04, 02/04, 03/04). One of those with a low bias, pair 01/02, has only a slight bias.

A)

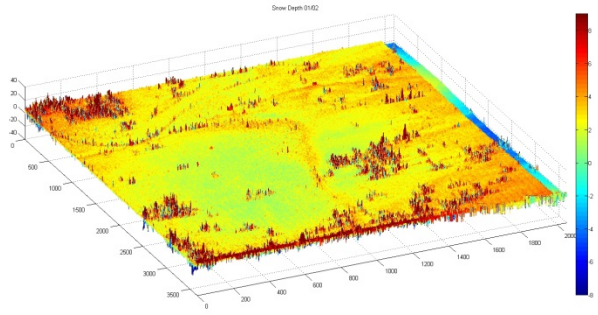

B)

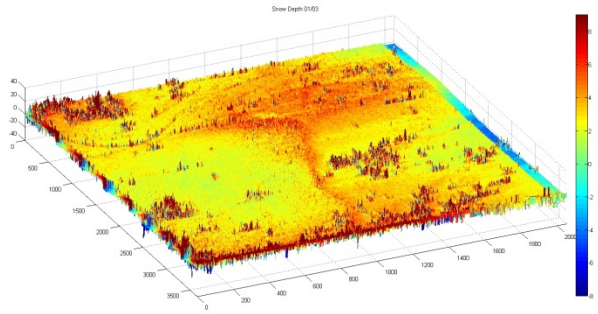

C)

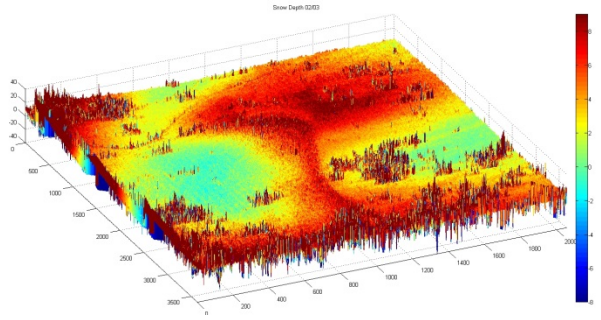

D)

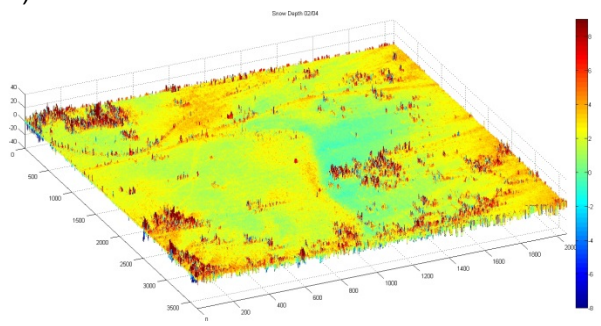

Figure 12: Mammoth Mountain Snow Depth images derived from the various InSAR pairs; A) 01/02, B) 01/03, C) 02/03, D) 02/04. The 02/03 pair shows unusually high snow depths compared to the rest, probably a bias (offset) of some kind in the BFPR.

Snow Depth Error by SAR image pair						
SAR Image Pair	01/02	01/03	01/04	02/03	02/04	03/04
Average Snow Depth error (cm)	-8.00	95.00	-49.06	175.69	-86.56	-41.69

Table 2: Compilation of average snow depth errors for the six InSAR image pairs.

An explanation of the snow-depth biases goes back to the fact that the flat earth phase is typically dominant in the unwrapped interferograms or the total phase images as opposed to the terrain phase and that it is the flight pair geometry or the baseline that determines the flat earth phase pattern. Examination of the total unwrapped phase in Figure 6 demonstrates this effect. Very little of the terrain phase can be seen in the total phase images. Often it is impossible to get even a sense of the underlying terrain.

The flat earth phase, both the range tilt and azimuth tilt, determined by the baseline, can be observed in each BFP (Figure 13).

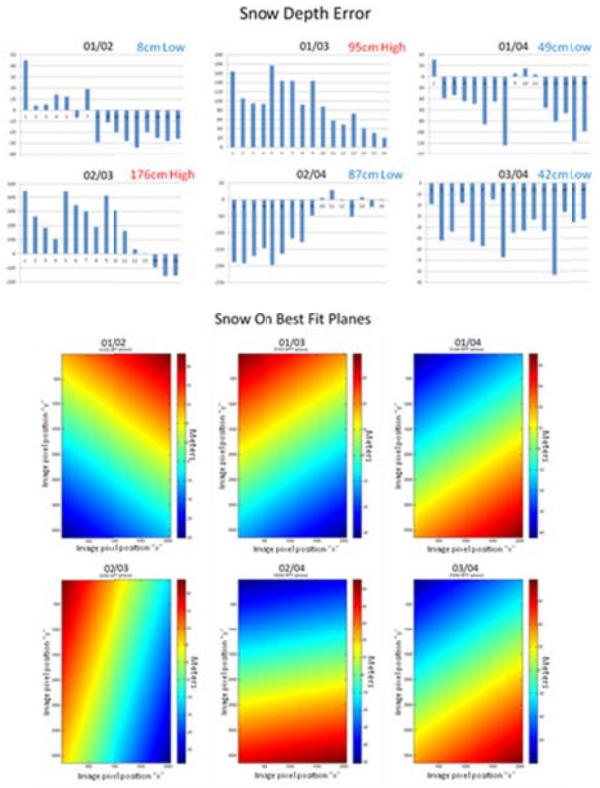

Figure 13: Relationship between the normalized snow depth error for each of the six interferometric image pairs and the pattern of the BFP derived from those interferograms.

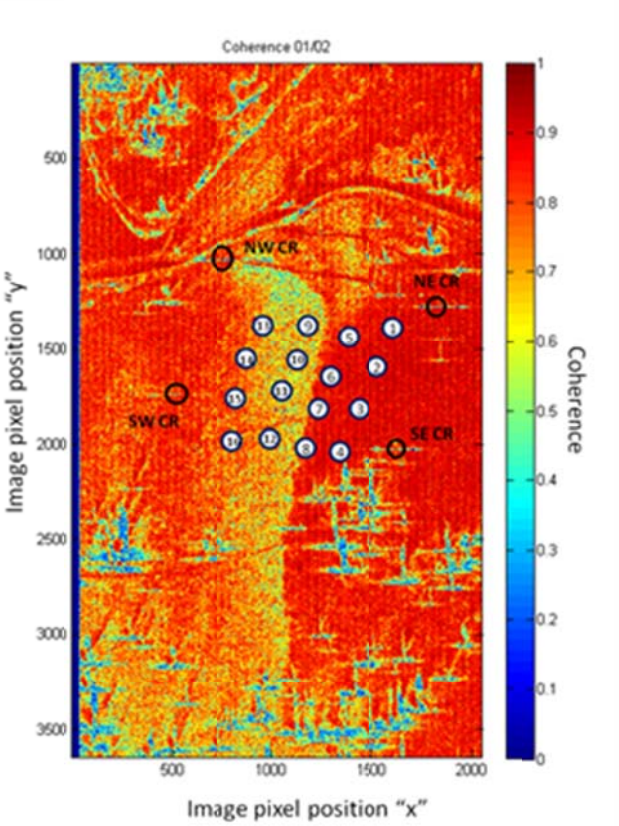

Figure 14: Coherence image for the 01/02 InSAR pair with the field validation snow depth sample sites.

For example, for SAR Image pair 01/02 (Figure 13), the range phase tilts up toward the north or away from the radar platform. In addition to that observation, the azimuth phase also tilts toward the east or the right side of the image area. Focusing on the azimuth phase and comparing it to the high and low average errors seems to indicate a pattern where the images with an eastward tilting azimuth phase demonstrate a low average error. Likewise, for those with a westward tilting phase there is a high average error. The mechanism behind this is not understood at this time.

The second bias noted involves both the coherence of the area in the image being looked at and the range phase tilt. Note that there is a distinct difference between the first eight snow depth locations and the second eight with respect to coherence. That can clearly be seen in Figure 14. The mechanism behind this is not understood at this time. The noted correlation does not prove causality; however it cannot be ignored and warrants further exploration.

The first 8 snow depth measurement locations have high coherence, ranging typically above 0.85 throughout the SAR image pairs. The second eight have lower coherence, typically averaging below 0.7, with the majority between 0.5 and 0.65, and some of the SAR image pairs as low as the mid-0.3 range. The exact reason for the low coherence in some of the SAR image pairs cannot be absolutely determined. It is however likely that this is due to low values in the magnitude of the returns at those particular locations. A quick comparison against the magnitude images seems to corroborate this. The strength of the magnitude of the radar return is typically due the surface properties and the incidence angle of the incoming radar emission. Snow radar reflectivity was observed to be significantly less than that of the solid ground. In addition to that, it appears that there are portions of the varying terrain that may be affected by a shallow incidence angle. A shallow incidence angle could be responsible for a decrease in the magnitude, and therefore be responsible for a decrease in the coherence. One other possibility is a difference in the liquid water

content of the snow surface as opposed to the frozen content. Generally, the higher the liquid content, the higher the expected reflectivity. This scenario seems unlikely though because east facing slopes should have a greater potential for melting than west facing slopes in the late morning hours when this area was imaged. The image area has a ravine running from the north to the south through the scene. The magnitude pattern seen is the opposite of what would be expected if there was disproportionate melting occurring. In other words, it is the west facing slope that has the greater magnitudes and the east facing slope has weaker magnitudes. Ultimately the important take away is that there is a distinct difference between the SAR coherency of the first eight and the second eight snow depth locations.

Two approaches were taken to explore these potential biases. The first was to examine relative coherence for the 16 sites in all 6 SAR image pairs with respect to the snow depth errors Again, note the pattern that differentiates the first eight snow depth locations from the second eight relative to coherence (lower coherence for the left 8 measurements, higher coherence for the right 8 measurements) (Figure 15). Second, the snow depth errors for each of the six pairs were normalized with respect to the average snow depth error, which was subtracted from the error at each of the measurement locations. This indicates how each individual location varied with respect to the average error. The results can be seen in Figure 16.

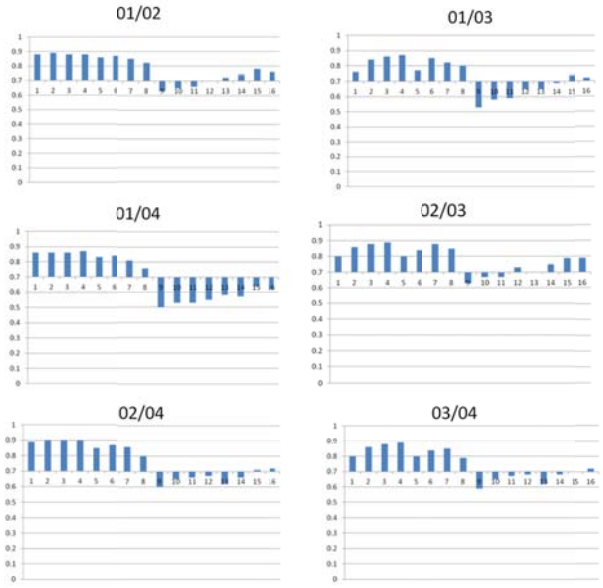

Figure 15: Average coherence per manual snow depth location for each of the six interferometric image pairs.

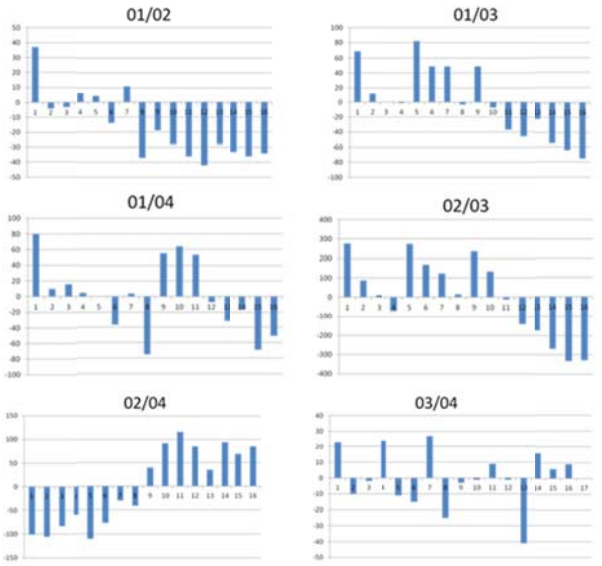

Figure 16: Normalized snow depth error per manual snow depth location for each of the six interferometric image pairs.

After the snow depth errors were normalized, it appeared that they generally follow the same pattern as that seen in the coherence images (Figures 14 – 16). In other words, after the normalization, the first eight show a high bias and the second show a low bias or the opposite configuration. It should be noted that this signal is not strong in all the cases such as SAR image pairs 01/04 and 03/4, while it is very strong in others. While the mechanism for this is not understood, it appears that there may be some relationship between this and the range phase, similar to that which was seen for the azimuth phase relative to the overall high or low average error. Compare Figure 16 to the BFP in Figure 13 and note that when the range phase slopes up toward the north; the first eight snow depth sites tend to be greater than the normalized line while the second eight tend to be less than the normalized line. When the range phase slopes toward the south or toward the radar platform the opposite is the case. The signal does tend to be weak in pair 03/04 and nonexistent in image pair 01/04. Again this does not show causality but the consistency of the pattern cannot be ignored. Therefore there appears to be a potential link to either the coherence, or the cause of the coherence pattern, and the particular flight geometry.

Another observation was made for three of the six SAR image pairs. In Figure 13, note that for image pairs 01/03, 02/03, and 02/04, the absolute snow depth errors show a stair-step pattern for every four measurements. This pattern is also

similar in SAR image pair 01/02, but the signal is not as strong. Each of these stairsteps corresponds with one of the rows in which the snow depths were manually measured. The lower position numbers indicate measurements further north or further from the radar, and the higher position numbers are further south, or closer to the antenna. For example, the eastward row of four snow depths had the "1" position as the most northerly component. Each successive location went south through location "4" and started over again at position "5" at the top of the collection scene on the next row (Figure 14).

In each of these four cases the snow depth error decreases as the position moves south. This held true for every row regardless of whether there was a high or low bias. It also held true regardless of the amount of coherence. There are a couple of possibilities that could account for this. The first one is that there may be an error in the overall slope of the underlying Snow-Off DEM. Recall that the Snow-Off DEM is subtracted from the Snow-On DEMs. An error in the average slope of the Snow-Off DEM may account for this pattern. The same pattern is not, however, apparent in the other two scenes, which likely negates this line of reasoning. Another potential explanation is that the error is contained in the slope derived from the 10m DEM. Recall that the 10m DEM slope was added back into both the Snow-On and Snow-Off BFPRL images. If the slope has the wrong tilt it would be indicated as an increase in error in a particular direction. The weakness to that argument is that the same wrong slope is added to both the Snow-On and Snow-Off images. That should cancel the error out when those images are subtracted from each other. Another potential source lies with the BFP generated in the Snow-On images. It is assumed that average elevation slope for the Snow-On image is the same as that of the Snow-Off. This would be a good assumption if the snow laid evenly across the scene. We know that is not entirely true. The BFPR images from the Snow-On cases may actually have a different average terrain slope. After the Snow-On BFPR is linearized, it is added back in to the 10m DEM slope. It is assumed that the BFPRL image is a deviation from the average slope and that the Snow-On and Snow-Off images have the same average slope. If in fact they don't, this will cause a regularly increasing error in a particular direction. For example, if the snow depth increases on average as one moves from the southern part of the image to the northern part of the image, the snow covered terrain slope will be steeper than that of the slope calculated from the 10m DEM. This would mean that there would be error in the slope that is added back in.

5 SUMMARY AND CONCLUSIONS

The goal of the SNODAR Project research was to explore the viability of using Multi-pass Single Look Complex InSAR to determine snow depth. The SAR datasets were acquired by General Atomics using a Lynx II radar an airborne platform. Differencing of a Snow-Off DEM and Snow-On DEMs derived from intereferometric Ku airborne data using a perturbation or decomposition of parts approach was used to estimate snow depth.

We developed a method that removed the flat earth phase and mean slope contributions to the InSAR measurements by estimating a best fit plane for an unwrapped phase image combined with the average slope derived from a low-resolution DEM. The Best Fit Plane Removal (BFPR) method bypassed the requirement for detailed, precise InSAR baseline knowledge by using the perturbation or decomposition approach to isolate the interferometric phase caused by the terrain that deviated from the mean slope. It also removed the flat earth phase that can be difficult to determine without the baseline information. A linear regression was applied to the BFPR image to convert phase to terrain elevation, which was then added back to the average slope, resulting in a DEM at the 0.1m resolution of the InSAR data. After computing DEMs from both Snow-On and Snow-Off scenes they were differenced to calculate snow depth.

The snow depth results for six Snow-On SAR pairs were compared to 16 manually measured snow depth locations with varying degrees of success. The SAR image pairs showed an average error of -8cm, 95cm, -49cm, 175cm 87cm and 42cm for the respective six SAR pairs. The results also indicated that coherence of the unwrapped InSAR image played a role in the DEM generation. Of the 16 manually measured locations, eight fell in a high coherence regime indicated by coherences greater than 0.7 and the others fell in a regime indicated by coherence less than 0.7. In almost all of the cases the magnitude of the error for each of the SAR image pairs fell into two categories determined by these regimes.

There did appear to be a consistent pattern of either high or low bias in the BFPR-calculated snow depth results. Four of the SAR image pairs demonstrated a low average for the snow depths while the other two pairs demonstrated a high average. This pattern indicates that errors may be either related to or driven by the BFPs produced

from the unwrapped interferograms. There appear to be two different biases. The first is that the slope of the azimuth aspect of the BFP affects the direction of the bias. It was observed that an eastward tilt in the BFP was consistent with SAR pairs with a bias towards low snow depth errors. Those with a westward tilt demonstrated a bias towards high snow depth errors. The second bias is not as well defined, but appears to relate to coherence in the data and the range slope of the BFP. After normalizing the error there was a clear difference between the snow depth locations with high and low coherence. Additionally, the determination of whether the high or low coherence was above or below the normalization line appeared to be controlled by the range tilt of the BFP. This pattern is not fully understood. Furthermore, the observed pattern does not necessarily indicate causality. Additional SAR image pairs need to be tested to confirm the pattern.

Another observation was made in four of the six SAR image pairs. It appeared that regardless of the coherence, the calculated error decreased as the observations moved southward or in the direction toward the sensor. This is indicative of a possible issue in the slope of one or more of the BFPR elements. Slope issues could arise from the calculation of the BFP, accuracy of the low resolution DEM used to determine the deviation of the high frequency terrain from the average slope, or an issue with representativeness of the low resolution DEM relative to the true slope of the snow covered terrain.

This research demonstrates that Ku-band radar is capable of discerning the snow air interface with minimal penetration and of therefore mapping snow depth. This is evident in both its ability to see features on the snow surface such as tracks in the snow from the researchers, the high coherence obtained, and the representative DEMs extracted that consistently showed the terrain or snow surface. The DEMs also consistently showed the Snow-On terrain to be higher than that of the Snow-Off terrain.

6 RECOMMENDATIONS FOR FUTURE WORK

While perfect results were not achieved, the BFPR method shows promise. The foundation has been laid for further investigation. The greatest challenge in this research was achieving good DEMs utilizing multiple SAR passes with an aircraft with only one antenna and an unknown baseline. SAR acquisition using an aircraft equipped with a bistatic antenna system with a frequency in the Ku-band or higher would greatly simplify the process and increase the probability of successful snow depth determination. While one of the main goals was to derive a method that could be used with operational monostatic platforms, it would benefit future research to test these techniques with a system that is better suited for DEM generation. The snow depth determinations would not then be dependent on the ability to derive DEMs using monostatic SAR platforms with the attendant baseline characterization problems. We are pursuing several research possibilities that use a bistatic InSAR approach. Once SAR interaction with the snow surfaces is better codified; the focus could transition to the operational platforms with only one antenna. These approaches should also be tested for a variety of snow conditions, as these affect radar returns from the surface and have the potential to affect the overall accuracy. Varying snow conditions from different times of the season with different properties should be explored to determine the effects on this technique.

7 ACKNOWLEDGEMENTS

We would like to thank Dr. Ralf Dunkel and the flight crews of General Atomic Aeronautical, who were instrumental obtaining the data used in this research. Without their support this project literally would not have been able to get off the ground.

Contributions made by Douglas Bickel at Sandia National Labs were also key to the success of this project. We would like to specifically acknowledge his input and guidance in developing mathematical approaches to the InSAR processing.

Alex Clayton of the Mammoth Mountain Ski Patrol played a critical role in determining the best location to conduct the research, helping to guide the on-mountain validation, and contributing extensively to on(in)-the-snow effort. Both Geoff Kruse and Maj. Paul Homan also spent many hours on the mountain digging holes and carrying equipment to the survey site. Without their efforts the research would not have been possible.

8 REFERENCES

AFWA (Air Force Weather Agency) 2012a: AFWA Algorithm Description Document (ADD) for the Air Force Weather Agency (AFWA) Snow Depth Analysis Model (SNODEP).

AFWA (Air Force Weather Agency), 2012b: AFWA Fact Sheet on Snow Depth and Sea Ice Analysis Model, [Available online at https://weather.afwa.af.mil/static/about_info/about_snow.html.].

Carrara, W. G., Goodman, R.S., Majewski R. M., 1995: Spotlight Synthetic Aperture Radar Signal

Processing Algorithms. 1st ed., Artech House, 554 pp.

Google Earth, “California.” Map. Google Maps. Web. Jun 2012: [Available online at http://www.google.com/earth/index.html.]

Evans, J. R., 2013, Determining Snow Depth using Airborne Multi-Pass Interferometric Synthetic Aperture Radar, Unpublished Ph.D. Dissertation, Naval Postgraduate School, Monterey, CA, 198 p.

Foster, J. L. et al., 2011: A blended global snow product using visible, passive microwave and scatterometer satellite data, International Journal of Remote Sensing, 32, 1371-1395

Goldstein R. M., Zebker H. A., and Werner C. L., 1988: Satellite radar interferometry: Two-dimensional phase unwrapping. Radio Science, 4, 713–720.

General Atomics Aeronautical, Sensor Systems, Lynx Multi-mode Radar, cited Dec 2012: [Available online at http://www.ga asi.com/products/sensor_systems/lynxsar.php.]

Hodgson, M. E., Jensen, J., Raber, G., Tullis, J., Davis, B. A., Thompson, G., Schuckman, K., 2005: An Evaluation of Lidar-derived Elevation and Terrain Slope in Leaf-Off Conditions. Photogrammetric Engineering & Remote Sensing, 71, 817–823.

Hopkinson, C., Sitar, M., Chasmer, L., and Treitz, P., 2004: Mapping Snowpack Depth beneath Forest Canopies Using Airborne LiDAR. Photogrammetric Engineering & Remote Sensing, 70, 323–330.

JPL (Jet Propulsion Laboratory), 2012a, SIR-C/X-SAR Flight Statistics, cited Aug 2012: [Available online at http://southport.jpl.nasa.gov/sir-c/getting_data/missions_stats.html.]

JPL (Jet Propulsion Laboratory), 2012b, What is SIR-C/X-SAR, cited Aug 2012: [Available online at http://southport.jpl.nasa.gov/desc/SIRCdesc.html.]

Marshall, H-P., Koh, G., and Foster, R. R., 2005: Estimating alpine snowpack properties using FMCW radar. Annals of Glaciology, 40, Issue 1, 157–162.

Marshall, H. P., Birkeland, K., Elder, K., and Meiners, T., 2008: Helicopter-Based Microwave Radar Measurements in Alpine Terrain. Proc. of the 2008 Int. Snow Science Workshop, Whistler, British Columbia, Canada, Telus Whistler Conference Center

Northrop Grumman, 2010: Algorithm and Data User Manual (ADUM) for the Special Sensor Microwave Imager/Sounder (SSMIS), Report-12621F CAGE/Facility Ident: 70143, 77 pp.

Osterhuber, R., Howle, J., and Bawden, G., 2008: Snow Measurement Using Ground-Based Tripod LiDAR. Western Snow Conference 2008. Hood River, OR.

Richards, J. A., 2009: Remote sensing with Imaging Radar. 1st ed. Springer-Verlag, 361 pp.

Rosen, P., 2009: InSAR Principles and Theory. UNAVCO Short Course Series- InSAR: An introduction to Processing and Applications for Geoscientists, Boulder, Colorado.

Shi, J. and Dozier J., 1996: Estimation of Snow Water Equivalence Using SIR-C/X-SAR. In IEEE, International Geoscience and Remote Sensing Symposium, Remote Sensing for a Sustainable Future, 4, 2002–2004.

Shi, J. and Dozier J., 2000a: Estimation of Snow Water Equivalence Using SIR-C/X-SAR, Part I: Inferring Snow Density and Subsurface Properties. IEEE Transactions on Geoscience and Remote Sensing, 38, 2465–2474.

Shi, J. and Dozier J., 2000b: Estimation of Snow Water Equivalence Using SIR-C/X-SAR, Part II: Inferring Snow Depth and Particle Size. IEEE Transactions on Geoscience and Remote Sensing, 38, 2475–2488.

Stofan, E.R, et al., 1995: Overview of Results of Spaceborne Imaging Radar-C, X-Band Synthetic Aperture Radar (Sir-C/X-SAR). IEEE Transactions on Geoscience and Remote Sensing, 33, 817–828.

Tsunoda, S. I., Pace, F., Stence, J., Woodring, M., Hensely, W. H., Doerry, A. W., and Walker, B.C., 1999: Lynx: A high-resolution synthetic aperture radar. SPIE Aeroense, 3704, 1–8.

Yankielum, N., Rosenthal, W., and Davis, R.E., 2004: Alpine snow depth measurements from aerial FMCW radar. Cold Regions Science and Technology, 40, 123–134.